On Suitability of ALOS-2/PALSAR-2 Dual-Polarized SAR Data for Arctic Sea Ice Parameter Estimation

Juha Karvonen, *Member, IEEE*, Eero Rinne, Heidi Sallila, and Marko Mäkynen, *Member, IEEE*

***Abstract*— In this article, ALOS-2/PALSAR-2 dual-polarized [horizontal-transmit–horizontal-receive and horizontal-transmit–vertical-receive (HH/HV)] ScanSAR mode L-band synthetic aperture radar (SAR) imagery over an Arctic study area was evaluated for their suitability for operational sea ice (SI) monitoring. The L-band SAR data are studied for the estimation of different SI parameters: SI concentration, SI thickness, SI type, and SI drift. Also, some comparisons with nearly coincident C-band data over the same study area have been made. The results indicate that the L-band SAR data from ALOS-2/PALSAR-2 are very useful for estimating the studied SI parameters and equally good or better than using the conventional operational dual-polarized C-band SAR satellite data.**

***Index Terms*— ALOS-2/PALSAR-2, dual polarized, L-band, synthetic aperture radar (SAR), sea ice (SI).**

I. Introduction

OPERATIONAL sea ice (SI) monitoring has mainly been based on C-band synthetic aperture radar (SAR) since the 1990s (ERS-1/2, ENVISAT/ASAR, RADARSAT-1/2, and Sentinel-1), and also, some X-band SAR instruments (TerraSAR-X, TanDEM-X, and COSMO-SkyMed constellation) have been used mainly as complementary information (for better temporal coverage). Previous studies have shown that the L-band SAR data can provide complementary information to the C- and X-band data, e.g., in [1]–[3]. The L-band is less sensitive to wet snow layer over SI, and it also has a deeper penetration depth in SI, thus being able to retrieve more information on the ice volume structure (volume scattering) than the C- or X-band SAR data. The L-band is also more sensitive to the degree of ice deformation and there is a higher backscatter contrast between the deformed and level ice at L-band. In general, the information content of the X- and C-band images is largely equivalent, whereas the L-band data are able to provide some complementary information.

Our objective is to study the SI parameter estimation based on the ALOS-2/PALSAR-2 L-band dual-polarized ScanSAR data. SI parameter estimation over the Baltic Sea using SAR imagery has extensively been studied at the Finnish Meteorological Institute (FMI) since the early 1990s. Baltic Sea is covered with a dense network of *in situ* measurements and daily ice charting, producing daily SI thickness (SIT), SI concentration (SIC), and degree of SI deformation, thus providing a good test bed for novel SI parameter estimation algorithms. FMI has also studied automated SI parameter estimation in other ice-covered sea areas, such as European parts of the Arctic ocean, Caspian Sea, Gulf of Saint Lawrence, and Bohai Sea. Our methods for SI parameter retrieval include SAR image feature extraction algorithms, SAR image segmentation algorithms, and both linear and nonlinear estimation algorithms based on segment-wise backscattering statistics (e.g., median or average) and texture features (see [4]–[8] for more details).

In this article, we have studied the possibilities to use the L-band dual-polarized SAR data with the horizontal-transmit–horizontal-receive and horizontal-transmit–vertical-receive (HH/HV) polarization combination for SI detection, and SI parameter estimation and classification. Five SI properties were specifically studied here: discrimination between SI and open water (OW), estimation of SIC, SI -type classification, estimation of SIT, and estimation of SI drift (SID). In addition to HH and HV backscattering coefficient magnitude (σ^0 or more specifically σ^0_{HH} and σ^0_{HV} for the HH and HV channels), several SAR texture features were studied. We have used the C-band Sentinel-1 SAR data, Russian ice charts, Norwegian ice model data, and SIC estimates based on microwave radiometers (MWRs) reference data sets.

II. Study Area and Data Sets Used in This Article

The FMI Arctic study area is located in the Kara and Barents seas. The study area is shown in Fig. 1. The coordinate system (CS) used in this article is the polar stereographic projection, with a center longitude of 55° E, reference latitude (latitude of the correct scale) of 70° N, and the WGS84 data. The upper left (UL) and lower right (LR) coordinates, given as polar stereographic CS northing and easting in meters, in this CS are the following: UL = (700 000, −1 100 000) and LR = (2 550 000, 1 100 000).

Totally, 138 ALOS-2/PALSAR-2 ScanSAR dual-polarization mode (HH/HV) images over the study area acquired during the period of January–August 2017 were included in this article. Our reference data set consists of Sentinel-1 C-band SAR data, Russian Arctic-Antarctic Research Institute

Manuscript received September 4, 2019; revised February 14, 2020 and March 25, 2020; accepted March 27, 2020. Date of publication April 27, 2020; date of current version October 27, 2020. This work was supported by the Japan Aerospace Exploration Agency (JAXA) 6th Research Announcement for the Advanced Land Observing Satellite-2 (ALOS-2) Project "Improved Sea Ice Parameter Estimation with L-Band SAR (ISIPELS)," PI number 3029 (PALSAR/PALSAR-2 data provided by JAXA), and under the European Space Agency (ESA) L-BAND SAR Applications and Requirements Consolidation Study under Contract 4000121573/17/NL/CT. *(Corresponding author: Juha Karvonen.)*

The authors are with the Marine Research Unit, Finnish Meteorological Institute, FI-00101 Helsinki, Finland (e-mail: juha.karvonen@fmi.fi).

Color versions of one or more of the figures in this article are available online at http://ieeexplore.ieee.org.

Digital Object Identifier 10.1109/TGRS.2020.2985696

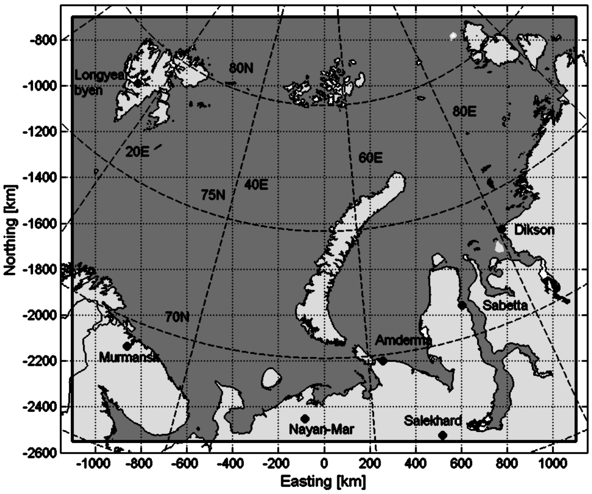

Fig. 1. Study area in Kara and Barents Seas.

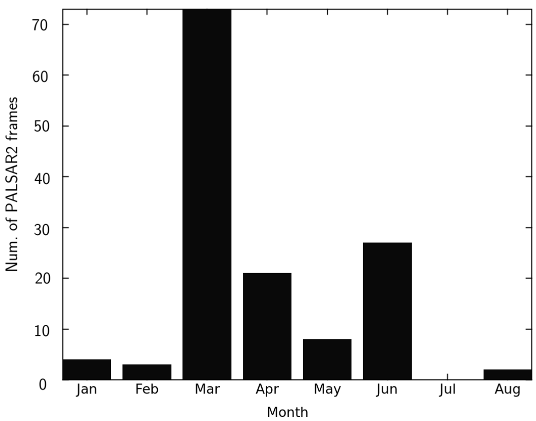

Fig. 2. Monthly distribution of the ALOS-2/PALSAR-2 imagery.

(AARI) ice charts (online: http://www.aari.ru/odata/_d0015.php), Advanced Microwave Scanning Radiometer 2 (AMSR-2) SIC [9], CryoSat-2 SIT [10], and TOPAZ4 ice model SIT [11]. The TOPAZ4 model data we use are the nowcast data, i.e., the first time step ($T = 0$) of each model run.

The monthly distribution of the ALOS-2/PALSAR-2 images is shown in Fig. 2. Most of the images (73 frames) were acquired during March 2017, but there were also a significant amount of images that were acquired in April (21) and June (27). The locations (bounding boxes) of the ALOS-2/PALSAR-2 images are shown in Fig. 3, and the month of image acquisition is indicated by the frame boundary color.

The data sets were divided into a training data set and test data set. The training data set consists of 30 randomly selected ALOS-2/PALSAR-2 SAR images and the corresponding reference data. The remaining 108 images were used as a test data set. The training data sets were used in defining the classification parameters, and all the classification results are given for the test data set in Sections II-A–II-C.

A. C-Band SAR Data From Sentinel-1

We used dual-polarized extra-wide (EW) swath Ground Range Detected Medium (GRDM) resolution mode Sentinel-1 SAR data with the HH/HV polarization combination over

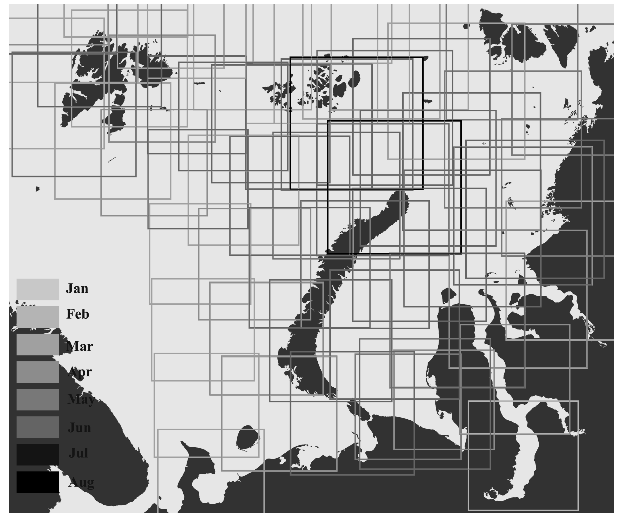

Fig. 3. Locations of the test ALOS-2/PALSAR-2 imagery in the study area, indicated by the image bounding boxes.

the study area as a reference C-band SAR data set. The Sentinel-1 data were georectified to our polar stereographic CS and were resampled into 500-m resolution. For compatibility, the comparisons to Sentinel-1 data sets were made in the 500-m resolution after downsampling the ALOS-2/PALSAR-2 imagery. The Sentinel-1 data were processed similarly as the ALOS-2/PALSAR-2 data, i.e., an incidence angle correction [12] was applied before georectification of the imagery.

B. Russian Ice Charts

The Russian Arctic ice charts are provided weekly by the AARI, located in St. Petersburg, Russia, on their web page (the English version on http://www.aari.ru/odata/_d0015.php?lang=1, last access: February 1, 2020). They are provided as thematic maps and in the SIGRID-3 vector format [13] in the polar stereographic projection with the midlongitude of 90°E. For this study, the AARI ice charts were reprojected into the polar stereographic CS used in this article. The ice charts contain information on the ice type, ice stage of development, and partial ice concentrations for the ice categories within each polygon identified by the ice analysts. SI attributes are attached to each ice chart polygon by the ice analysts. The attached attributes are described by the polygon-wise World Meteorological Organization (WMO) SI egg code [14], [15], and the ice parameters used in this article have been derived from these polygon attributes. The nominal resolution of ice charts is typically about 1 km, but this only applies for the polygon boundaries, the polygons are typically rather coarsely drawn and only give information on the outlines of the ice situation within a polygon, and many SI details within polygons have been ignored. This can be understood in the light that the ice analysts draw ice charts over vast areas and have tight schedules for the ice chart completion. The ice thickness values used in this article are weighted averages of the average ice thickness of the ice stages of development within each polygon, the weights in the weighted average calculation being the proportion of

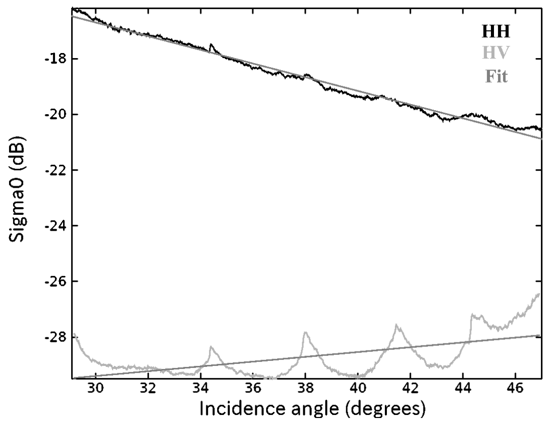

Fig. 4. ALOS-2/PALSAR-2 statistical incidence angle dependence for HH (red curve) and HV (blue) channels and their linear LSs fits (green).

each stage of development class within the polygon. As ice thickness for a stage of development class in the ice charts is given as a thickness range, we have used the midrange value of each thickness range in our computations. The ice classes used, here, in the ice classifying experiment are the major (mode) ice classes for each polygon. The classes used in this article are shown in the legend of Fig. 12: OW, nilas ice (NI), young ice (YI), first-year ice (FYI), old ice (OI), and land-fast ice (LFI).

C. Preprocessing of ALOS-2/PALSAR-2 Data

The ALOS-2/PALSAR-2 data were first calibrated according to the guidelines given in [16]. Then, the ALOS-2/PALSAR-2 SAR data were georectified to our polar stereographic CS in 100-m resolution.

Before any classification or estimation tests, we performed a statistical analysis of the incidence angle dependence for the ALOS-2/PALSAR-2 training data set. The analysis was performed over the ice-covered areas of the training data set imagery (SIC over 80% according to the AMSR2-based SIC estimation using the methods presented in [17]). At the HH channel (log scale), σ^0 has a linear incidence angle dependence on the incidence angle with a slope of -0.246 for SI defined by a least-squares (LSs) fit (see Fig. 4, red curve). The slope is very similar as for C-band (RADARSAT-2, Sentinel-1) HH channel [18], [19]. At the HV channel, the incidence angle dependence is more complex, mainly due to the varying noise floor along the range. A surprising property was that the average backscattering at the HV channel was even slightly increased as a function of increasing incidence angle for the training data set (a slope of 0.085 based on the LS fit) as a function of the incidence angle. Also, the noise floor variation within the PALSAR-2 subswaths is clearly visible in the HV channel plot of Fig. 4 (blue curve).

A linear incidence angle correction for our ALOS-2/PALSAR-2 HH channel data was then applied, using the detected slope (-0.246). For the HV channel, no incidence angle correction was applied. The SAR data were then also downsampled to 500-m resolution (pixel size) for segmentation. Finally, a land mask based on the Global Self-consistent, Hierarchical, High-resolution Geography (GSHHG) Database coastline data set [20] was applied to the SAR images to exclude land areas from the computation.

III. METHODOLOGY

To classify SAR imagery or to extract SI parameters, the pixel-wise SAR backscattering coefficients (σ^0) are not very useful. This is because of the speckle noise present in SAR imagery and also due to the fact that different types of SI in many cases have wide and overlapping σ^0 distributions. Better results can be achieved by utilizing texture features computed from the SAR σ^0 images in addition to filtered σ^0 values. In our case, the filtering is performed by first applying a segmentation to the imagery and then using segment median values instead of single SAR pixel values. Segment median was applied for both σ^0 data and SAR texture features.

The downsampled (500 m) images were first segmented using the iterated conditional mode (ICM) algorithm [21]. The segmentation was applied to the principal component (PC) image of the two SAR polarization channels. After the ICM segmentation segments, smaller than 100 pixels were merged to the neighboring segment with the closest PC image segment median. This was done to reduce the random variation due to speckle noise.

Multiple texture features were computed from the SAR data. The texture features were computed within each SAR segment using the 100-m resolution and assigned to each segment in the 500-m resolution. The texture features computed for each segment and separately for both HH and HV channels were autocorrelation (C_A), entropy (E), local signal-to-noise ratio (SNR), variogram slope V_1, and HH/HV cross correlation (C_C). The segment-wise median values of each texture feature were used in our experiments here.

The features were computed in a round-shaped sliding window W with a diameter of 11 pixels (i.e., the window has a radius R of 5 pixels and has an odd size diameter such that it has a center point in the middle of a pixel location). The total number of pixels in the window was 81 pixels.

Entropy E [22] was computed as

$$E = -\sum_{k=0}^{255} p_k \log^2 p_k \tag{1}$$

where p_k values are the proportions of each gray tone k within each computation window W. Autocorrelation C_A was computed as

$$C_A(k,l) = \frac{\sum_{ij\in W}(I(i-k,j-l)-\mu_W)(I(i,j)-\mu_W)}{N\sigma_W^2} \tag{2}$$

where $I(i,j)$ is the pixel value at location (i,j), i and j refer to the row and column coordinates of the image pixel, respectively, and k and l here refer to the displacement of the row and column coordinates from (i,j), respectively. Mean over the directions horizontal, vertical, and diagonal directions, i.e., $(k,l) = (0,1)$, $(k,l) = (1,0)$, $(k,l) = (1,1)$, and $(k,l) = (1,-1)$ was used because the statistic C_A describes 2-D data [23], [24]. The size of the computation window W in pixels is denoted by N ($N = 81$). μ_W and σ_W are the window pixel value mean and standard deviation, respectively.

The cross correlation C_c between the SAR HH and HV channels, denoted by I_{HH} and I_{HV}, respectively, is

$$C_c(k,l) = \frac{1}{N\sigma_{\mathrm{HH}}\sigma_{\mathrm{HV}}} \times \sum_{i,j\in W}(I_{\mathrm{HH}}(k+i,l+j)-\mu_{\mathrm{HH}})(I_{\mathrm{HV}}(k+i,l+j)-\mu_{\mathrm{HV}}) \quad (3)$$

where N ($N = 81$) is the number of pixels within the computation window W. Round-shaped windows with $R = 5$ were again used for C_c. The mean values μ_{HH} and μ_{HV} are computed as averages of the pixel values within W.

SNR was estimated within a data window W by dividing the data window average (μ_w) by the data window standard deviation (σ_w)

$$\mathrm{SNR} = \mu_w/\sigma_w. \quad (4)$$

We also computed certain features based on variograms that also described the spatial autocorrelation in a slightly different manner. The variograms were also locally estimated, again in a round-shaped window W with $R = 5$ pixels using the original georectified SAR resolution (100 m); the computation was performed in five pixels steps such that the result became downsampled to 500-m resolution. Assuming a stationary and isotropic process, the variogram γ is (locally) dependent only on the interdistance (h) and can be estimated as [25]

$$\gamma(h) = \frac{1}{2|N_h|}\sum_{i,j\in N_h}|I_i - I_j|^2 \quad (5)$$

where I_i and I_j are the pixel values at locations i and j, whose distance is h, N_h is the set of pairs of observation z with indices k and l such that $|I_k - I_l| = h$, and $|N_h|$ is the number of such pairs. We modeled the range of the variogram from the origin (nugget) to the sill by fitting a linear variogram as a function of h on this interval. The slope and intercept value of the linear fit can be used as SAR texture features. The slopes and intercepts are referred here as V_1^{ch} and V_2^{ch}, respectively, where the superscript ch is the SAR channel, either HH or HV. However, here, we have used only V_1 because V_2, at least alone, does not have a very good performance in distinguishing between SI classes.

IV. Comparison Between L-Band and C-Band Data

We first performed a comparison between the L-band data and the corresponding C-band data over the area of each ALOS-2/PALSAR-2 image acquired during the same day as the PALSAR-2 images. The common areas of Sentinel-1 and PALSAR-2 data were that cropped from the same day images. This was performed in the 500-m resolution that is the resolution of the FMI operational SI products (SIC and SIT, [17], [26]) and thus had the 500-m C-band SAR data easily available. The main idea of this intercomparison was to compare how well details can be distinguished in the L-band imagery of SI (and included OW areas) and the correspondence to C-band imagery over the same area. For this purpose,

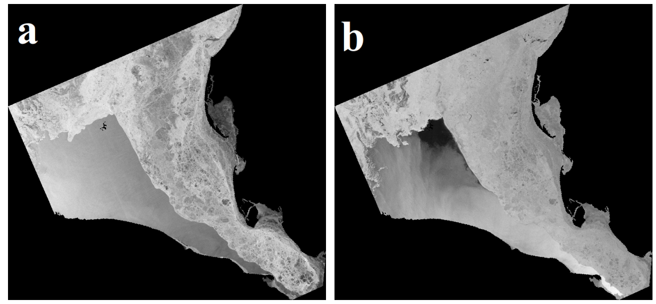

Fig. 5. (a) Typical example of an HH channel of ALOS-2/PALSAR-2 and (b) cropped Sentinel-1 image of the same day over the ALOS-2/PALSAR-2 image area, March 26, 2017.

we computed the σ^0 standard deviation, kurtosis, histogram width (from 5% to 95% of the histogram values), and average gradient for each L-band image and the corresponding cropped C-band data in the 500-m resolution. The results were computed separately for HH and HV polarization channels. The gradient was computed at each 500-m SAR pixel as the maximum absolute value of the differences between the center pixel and its eight neighboring pixels. The average gradient was then computed based on these pixel-wise gradient grids.

Here, we only discuss on the average values of the above-mentioned quantities. The average HH σ^0 standard deviations (3.0 dB for L-band and 2.9 dB for C-band) did not differ significantly between the L- and C-bands. The HH kurtosis for the L-band and the C-band σ^0 data was 0.04 and 0.29, respectively, indicating that the distributions of both the bands were mostly slightly super-Gaussian and for C-band more super-Gaussian. Naturally, there were larger variations between single images (C-band from about −1 up to 14 and L-band from about −1 to 6). The HH histogram widths were quite similar to L-band and C-band data, on average a little over 9 dB. However, the average HH channel gradient value for L-band (1.5 dB) was higher than that for C-band (1.3 dB), indicating that the L-band is able to distinguish more details than C-band at HH polarization. For the HV polarization, the differences were more apparent than for HH. The L-band HV σ^0 standard deviation was significantly higher than for C-band (3.2 versus 1.8 dB), and L-band histogram width was also significantly larger than for C-band (9.9 versus 5.6 dB) as well as the average gradient (1.35 versus 0.96 dB). The average kurtosis values were some above three for both L- and C-band HV data. These numbers indicate that significantly more details and more distinguishable edges over SI can be found in L-band imagery compared with the C-band imagery. This was also confirmed by visual inspection of the corresponding L- and C-band imagery.

As an example in Figs. 5 and 6, an example of the ALOS-2/PALSAR-2 L-band and the corresponding day's overlapping Sentinel-1 C-band image HH (see Fig. 5) and HV channels (see Fig. 6) of March 26, 2017, is shown. There was a time difference of about 12 h between the L- and C-band images, and some ice drift near the ice boundary had occurred during this period, but basically the same ice fields can be seen and compared in both the SAR images. The contrast difference between the C- and L-bands is visually clear for

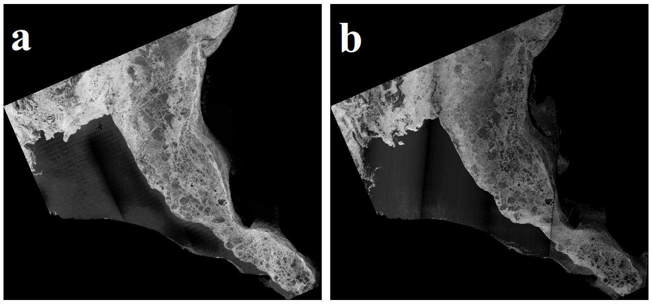

Fig. 6. (a) HV channel of ALOS-2/PALSAR-2 and (b) cropped Sentinel-1 HV channel image of the same day, March 26, 2017, corresponding to the HH channel images in Fig. 5.

both the polarization channels, and more ice details can be seen and extracted in the L-band channel images. It can also be seen that the HH backscattering from OW overlaps with the backscattering from sea ice for both L- and C-bands. There are bright OW areas in both the channels in the areas where the waves have a suitable wavelength and direction with respect to the SAR instrument to produce strong Bragg scattering. This is the reason why backscattering cannot directly be used to distinguish between SI and OW. The air temperature during March 26, 2017, in the area was around $-5°$ according to the National Centers for Environmental Prediction/National Center for Atmospheric Research (NCEP/NCAR) model [27] reanalysis data, and also, the temperatures during the period before the SAR acquisitions were below zero, so there was no wet snow or water on SI on March 26, 2017.

V. Studied SI Parameters and Difference Measures Used in Evaluation

In this article, we specifically studied the discrimination between SI and OW, SIC estimation, SIT estimation, SID estimation, and SI-type classification based on our ALOS-2/PALSAR-2 L-band SAR data set. Ice concentration can be estimated based on the SI/OW discrimination using a sliding window and counting the OW and SI pixels within the window or by applying analysis based on segment-wise SAR texture features. SIT estimation studied here is also based on the segment-wise SAR texture features. We also performed a test of ice drift estimation using the only properly overlapping image pair with a reasonably short-time difference between the SAR image acquisition times and the detectable ice drift (very large drift cannot be detected anymore as the algorithm search area is limited). SI/OW discrimination is studied in Section V-A, SIC estimation in Section V-B, SIT estimation in Section V-C, and SID estimation in Section V-D.

In the comparisons made to evaluate the performance of the presented ice parameter estimation methods, we have used the following measures of difference between the L-band estimate and reference data sets:

$$\mathrm{RMSD} = \sqrt{\frac{\sum_{i=1}^{M}\left(X_i - X_i^{\mathrm{ref}}\right)^2}{M}} \tag{6}$$

$$D_{L1} = \frac{1}{M}\sum_{i=1}^{M}\left|X_i - X_i^{\mathrm{ref}}\right| \tag{7}$$

$$D_{\mathrm{sgn}} = \frac{1}{M}\sum_{i=1}^{M}\left(X_i - X_i^{\mathrm{ref}}\right). \tag{8}$$

M refers to the number of samples (number of grid points) used in the comparison and X_i ($i = 1, \ldots, N_c$) are the estimated values of the parameter (e.g., SIC or SIT) and X_i^{ref} are the values of the reference data at the same location as X_i. RMSD is the root mean-squared difference, D_{L1} is the L1 difference, and D_{sgn} is the signed L1 difference giving the estimation bias, positive bias indicating overestimation and negative bias indicating underestimation.

We have also used the correlation R_c as a measure of similarity of two pairwise ordered data sets, i.e., sets of pairs of estimated value and reference data value at the same locations

$$R_c = \frac{1}{M\sigma_x\sigma_{\mathrm{ref}}}\sum_{i=1}^{M}(X_i - \mu_x)\left(X_i^{\mathrm{ref}} - \mu_{\mathrm{ref}}\right) \tag{9}$$

where μ_x and μ_{ref} are the means of the estimate values and the reference values, respectively, and σ_x and σ_{ref} are the standard deviations of estimate values and the reference values.

A. Discrimination Between OW and SI, SIC

The reference data were extracted from the FMI AMSR-2 SIC estimation algorithm [17] using ALOS-2/PALSAR-2 segmentation by the ICM algorithm and then assigning an SIC value to each segment. Classification to OW/SI was made using the following thresholding: SIC $< 0.2 \rightarrow$ OW and SIC $> 0.8 \rightarrow$ SI, and the rest of the data, representing a mixture of SI and OW, were excluded.

Based on the training data set, a Bayesian threshold for σ^0 and each SAR texture feature was defined, and the discrimination capability of applying these thresholds was estimated. The Bayesian classification rule in case of N_c classes C_k with $k = 1, \ldots, N_c$ and with a data vector X is

$$c = \mathrm{argmax}_{k=1\ldots N_c} P(x|c_k)P(c_k) \tag{10}$$

where $P(x|c_k)$ is the value of the class c_k PDF at x and $P(c_k)$ is the prior probability of the class c_k such that $\sum_{k=1}^{N_c} P(c_k) = 1$. Here, as we have used only one feature at a time, x is just a single value and normalized histograms have been used as the PDFs.

The discrimination results for C-and L-band σ^0 and single L-band texture features are presented in Table I.

According to the performed tests, σ^0 is not a particularly good OW/SI discriminator at neither L- nor C-band. HV σ^0 performs some better than HH σ^0. The best texture feature discriminators were HH autocorrelation (0.88), HH entropy (0.84), and HH variogram slope (0.84). The best HV channel discriminators were autocorrelation (0.83), followed by entropy (0.79). In the Bayesian thresholding, we here simply assumed equivalent prior probabilities ($P(C_1) = P(C_2) = 0.5$) for SI and OW.

In Fig. 7, the histograms of ALOS-2/PALSAR-2 HH autocorrelation and HH entropy for the two classes (SI and OW) are shown. It can be seen that most of the OW can be distinguished from SI since it has a low texture value, but there still are some OW data points overlapping with the SI class.

TABLE I

OW/SI DISCRIMINATION POWER OF SELECTED TEXTURE FEATURES USING A BAYESIAN THRESHOLDING

Method	OW	SI	total
σ^0_{HH} (L-band)	0.22	0.86	0.60
σ^0_{HV} (L-band)	0.17	0.99	0.66
σ^0_{HH} (C-band)	0.55	0.70	0.62
σ^0_{HV} (C-band)	0.82	0.70	0.76
E_{HH}	0.70	0.94	0.84
E_{HV}	0.69	0.85	0.79
C_A^{HH}	0.79	0.94	0.88
C_A^{HV}	0.77	0.87	0.83
C_C	0.62	0.80	0.72
V_1^{HH}	0.78	0.89	0.84
V_1^{HV}	0.74	0.70	0.72
SNR_{HH}	0.11	0.99	0.59
SNR_{HV}	0.17	0.98	0.65

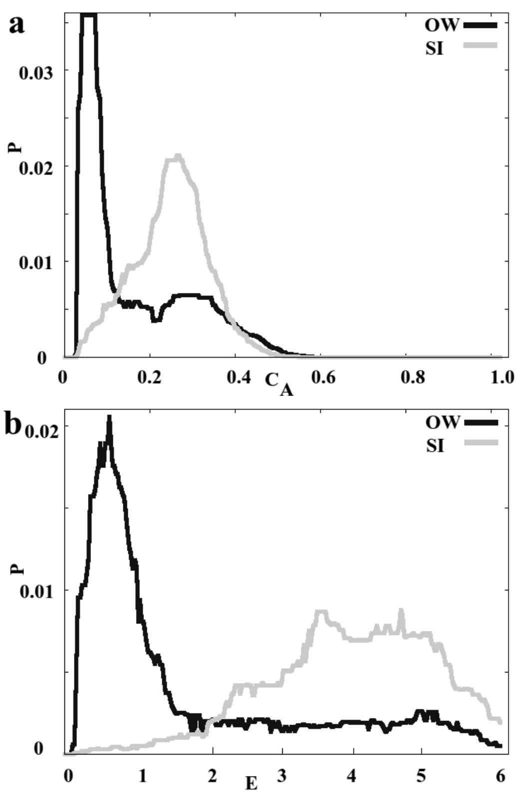

Fig. 7. (a) Histograms for the ALOS-2/PALSAR-2 HH autocorrelation and (b) HH entropy.

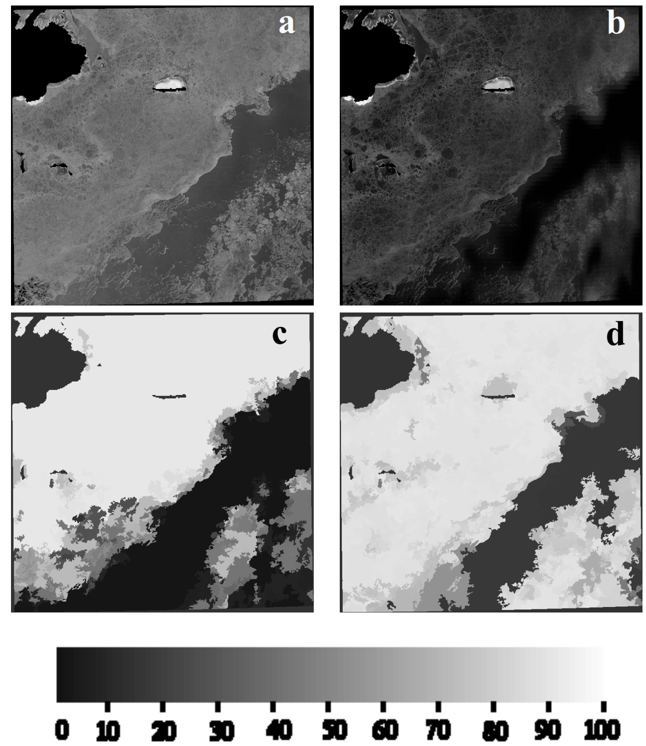

Fig. 8. (a) ALOS-2/PALSAR-2 HH channel and (b) HV channel on 8 June 2017 (©JAXA) and the corresponding SIC estimate based on (c) AMSR2 MWR data and (d) PALSAR-2 data. SIC is given in percent.

TABLE II

ERROR MEASURES FOR THE MLP SIC ESTIMATION, THE UNIT IS PERCENTAGE POINT

Data set	Bias (D_{sgn})	L1 difference (D_{L1})	RMSD
Train	1.7 (5.6)	7.9 (5.8)	13.1 (7.9)
Test	3.2 (9.9)	10.8 (8.6)	17.1 (10.8)

We also studied the estimation of SIC based on a multilayer perceptron (MLP) neural network using a similar algorithm as introduced in [8] for C-band SAR. To train the MLP, we used the error backpropagation algorithm. The number of hidden layer neurons was 11 in our experiment. The training and reference data used here were based on the SIC estimated from AMSR2 MWR data for each SAR segment (see [17] for details). Table II shows the estimation errors for the training and test data sets, and the values in parentheses are standard deviations. An example of the SIC estimation based on the method for one ALOS-2/PALSAR-2 image of the test data set is shown in Fig. 8, and also, the corresponding AMSR2 SIC estimation is shown in Fig. 8. This ALOS-2/PALSAR-2 image is from early June and at that time of the year ice is already in the melting stage. Compared with our visual interpretation, AMSR2 SIC is underestimated in some areas. In this case, L-band SAR SIC estimation seems to work better. The SIC underestimation by the MWR algorithm is based on the change of brightness temperature due to wet snow cover and liquid water on top of the SI [28]. It seems that L-band SAR is less sensitive to wet snow cover than MWR. D_{sgn}, i.e., bias between the ALOS-2/PALSAR-2 SIC estimate and the MWR SIC was in the range −1.8–2.8 percentage points during January–May but in June it was 31.8 percentage points, indicating that the SAR SIC was on average that much higher. Also, the correlation between SAR and MWR SIC dropped from the values around 0.90 in January–May to 0.46 in June–August and D_{L1} from 7.8 to 37.4 percentage points.

The values in Table II are some better than those reported for C-band SAR over the Baltic Sea in [8]. However, it should be noted that in [8], SIC from Baltic SI charts was used for training. It should also be noted that the data include the melting period data (June–August), and during the melting period, the AMSR2 SIC is often underestimated, thus affecting the SAR-based estimation results also through the incorrect training.

B. SIT and SI Volume

We also studied the estimation of SIT based on SAR data. For training, the SIT estimation we used our ALOS-2/PALSAR-2 training data set and the corresponding CryoSat-2 (CS-2) SIT estimates. The CS-2 thickness data were assigned to SAR segments as segment medians of the CS-2 estimates of the same day within the segment. Only segments with 11 or more CS-2 samples during the same day of assigning the SAR image were included in the comparison. This was done to get more reliable CS-2-based SIT estimates for the SAR segments. The algorithm used in the CS-2 SIT estimation is described in detail in [29].

There were 17 ALOS-2/PALSAR-2 images with an AARI ice chart of the same day in our test data set, and we use this subset for evaluating our SIT estimation here. We first studied the correlation of single SAR features and SIT from CS-2 assigned to SAR segments, but not a very high correlation (R_c) between any single SAR texture feature and SIT was found. The most significant features with this respect were E_{HH}, C_A^{HH}, V_1^{HH}, $\mathrm{SNR}_{\mathrm{HH}}$, and $\mathrm{SNR}_{\mathrm{HV}}$. The range of R_c for these single features was from 0.2 to 0.36. Then, we studied a linear combination of the five most significant features based on a PC analysis (PCA). The features selected based on PCA were E_{HH}, C_A^{HH}, V_1^{HH}, $\mathrm{SNR}_{\mathrm{HV}}$, and $\mathrm{SNR}_{\mathrm{HH}}$. Because there were no *in situ* SIT measurement available, the reference data sets used were the segment-wise CS-2 SIT (also for training), AARI ice chart SIT, and TOPAZ4 ice model SIT.

We tested the SIT estimation performance with our ALOS-2/PALSAR-2 test data set. The correlation R_c between the reference SIT from CS-2 and the estimation was $R_c = 0.54$ for the test data set and the corresponding L1 difference was $D_{L1} = 22.4$ cm using our independent test data set. When compared to AARI SIT, $R_c = 0.41$ and $D_{L1} = 18.0$ cm, and to TOPAZ4 model, SIT $R_c = 0.54$ and $D_{L1} = 19.8$ cm. We also made a similar test for C-band SAR data over the same area. The results were inferior compared with the L-band results, the L1 differences with respect to AARI SIT and TOPAZ4 SIT were reasonable (18.7 and 22.2 cm), but the correlations were very low for both the comparisons, around 0.15. An example of an ALOS-2/PALSAR-2 HH channel image HH, the SIT estimate based, and the corresponding AARI ice chart and TOPAZ4 ice model SIT are shown in Fig. 9. This SAR image covers an area northeast of the Novaya Zemlya island (northeastern part of the island can be seen in the SAR image as a white mask area). It can be seen that both the AARI and TOPAZ4 SIT have very little local variation and only give a very general view of the ice thickness.

SI volume over an area W can be computed when SIC (C) and SIT (H) over the area are known in a straightforward manner

$$V_{\mathrm{ice}} = A_p \sum_{(r.c)\in W} C(r,c)H(r,c) \tag{11}$$

where A_p is one product grid cell (pixel) area (0.25 km^2 in our 500-m grid). Based on the L1 accuracy estimates for SIC and SIT, we can roughly estimate the accuracy in estimating V_{ice}. The accuracy of the derived quantities, such as ice volume, can be estimated based on the multivariate Taylor expansion. If we further assume that the errors are relatively small, we can also assume the higher order terms to be neglectable and estimate the error (roughly) only by the first-order terms. If the derived quantity here is V_{ice}, then the first-order estimation error or accuracy ΔV_{ice} can thus be estimated as [30]

$$\Delta V_{\mathrm{ice}} \approx A_p(C\Delta H + H\Delta C). \tag{12}$$

If we, for example, assume 2-m-thick ice and 100% ice concentration and using L_1 differences of C and H with respect to reference data $\Delta H = 0.2$ m and $\Delta C = 0.11$ (11 percentage points), we get a relative accuracy of about 20% for the ice volume estimates based on the ALOS-2/PALSAR-2 data with these assumptions. For thinner ice, the relative uncertainty would then be some larger, e.g., for 1-m SI around 30% assuming a high SIC.

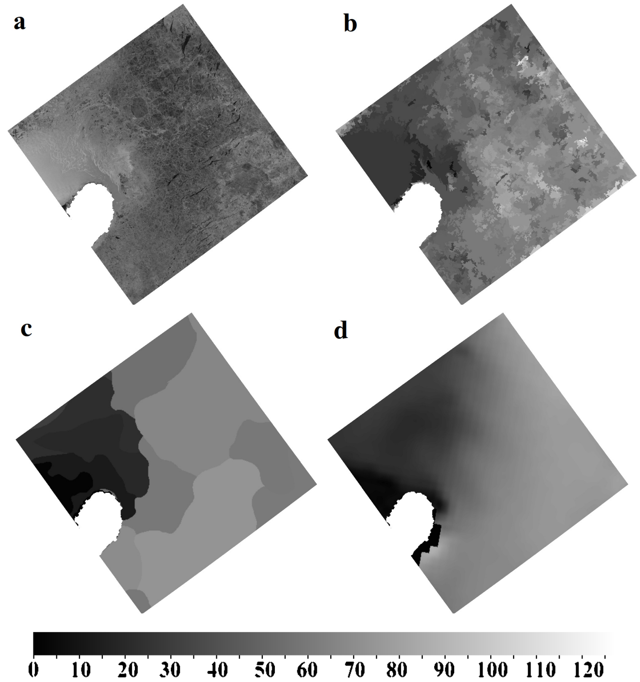

Fig. 9. (a) ALOS-2/PALSAR-2 HH channel, March 14, 2017 (©JAXA). (b) SIT estimate. (c) SIT derived from AARI ice chart. (d) SIT from TOPAZ4 ice model. Ice thickness unit in the color mapping is cm.

C. SI Type

We also studied the possibility to perform a SI-type classification based on the available ALOS-2/PALSAR-2 data. We used the ice typing of AARI ice charts as a basis for the classification and computed single feature histograms corresponding to the six classes of the AARI ice charts for our training data set. We excluded the LFI class because this class is defined differently from the other classes, i.e., based on its static nature, and it can include a large variety of ice types if classified based on the criteria applied to other ice fields. The AARI ice classes studied here were OW, NI, YI, FYI, and OI present in the AARI ice charts over the study area. We again noticed that SAR σ^0 is not at all useful for SI-type classification neither at HH nor HV channel. Texture features had a better distinguishing performance between the ice classes, and the best-performing single texture feature for ice-type classification was the HH variogram slope, V_1^{HH}. It is quite obvious that the classification can be improved to a certain extent by including more complementary features, e.g., HV channel features complement the HH features. However, we have not performed such experiments here but only studied the performance of single SAR features in ice-type classification. We noticed that a good separation of all the six classes is impossible based on the dual-polarized SAR data. This may partly be due to the coarse accuracy of the training data (AARI ice charts) and also due to the fact that the classes used in ice charts are not best suitable for detection based on the L-band or C-band SAR data. For example, degree of ice deformation [31] would be a better parameter to be estimated based on the SAR data. Unfortunately, we do not have any reference data over our study area for evaluating this. Histograms of σ_{HH}^0 and V_1^{HH} are shown in Fig. 10. The V_1^{HH} histogram suggests that three or four classes (including OW) could rather well be distinguished, but the remaining classes would mainly be mixed with the distinguishable classes. For comparison in Fig. 11, the same histograms for the Sentinel-1 C-band SAR data are shown. It can be seen that the σ_{HH}^0 histograms of the classes for C-band are overlapping and C-band σ_{HH}^0 cannot be used for classification. It can also be seen that the class-wise C-band V_1^{HH} histograms overlap significantly more than for L-band and this texture feature is neither suitable for SAR classification at C-band.

It should also be noted that the classes derived from SAR imagery do not directly correspond to the classes available in ice charts. The classes derived from SAR imagery rather describe the physical properties of the SI surface layer (to the electromagnetic radiation penetration depth), and only some SI classes present in ice charts can directly be derived from the SAR classes, such as level ice/smooth ice and deformed (older) ice which has gone through deformations and thus has a rougher surface compared to new ice. SAR classification can also provide additional classes that are not described in ice charts (such as different classes of deformed ice).

We tested a classification scheme based on the (optimal) Bayesian thresholding of V_1^{HH}, which seemed to have the best ability to distinguish between the given classes based on the histogram for the training data set. LFI class (white) was not included in our classification as it is difficult to distinguish from other classes. However, it can be rather reliably identified based on temporal cross correlation of multitemporal SAR imagery [32] if there is a dense enough temporal SAR cover over the study area. We again used equivalent prior probabilities (weights) for the ice classes. Applying more truthful prior class weights would likely have improved the classification. However, defining such realistic weights, which are dependent on the time and location, would require a larger comprehensive training data set, preferably covering a time period of several years. In our experiment using V_1^{HH} alone and Bayesian thresholding to distinguish between the ice classes, the OW class (blue in Fig. 10), FYI class (yellow), and OI class (red) were best distinguished, the overall correct classification being 55%, 79%, and 72% compared with the AARI ice charts of the same day (totally, 17 ALOS-2/PALSAR-2 images acquired during the weekly ice chart dates were found in our data set). For the other classes, the classification rates were worse (31% for nilas and 29% for YI). Two examples of the ice-type classification based on the Bayesian thresholding of V_1^{HH} are shown in Fig. 12.

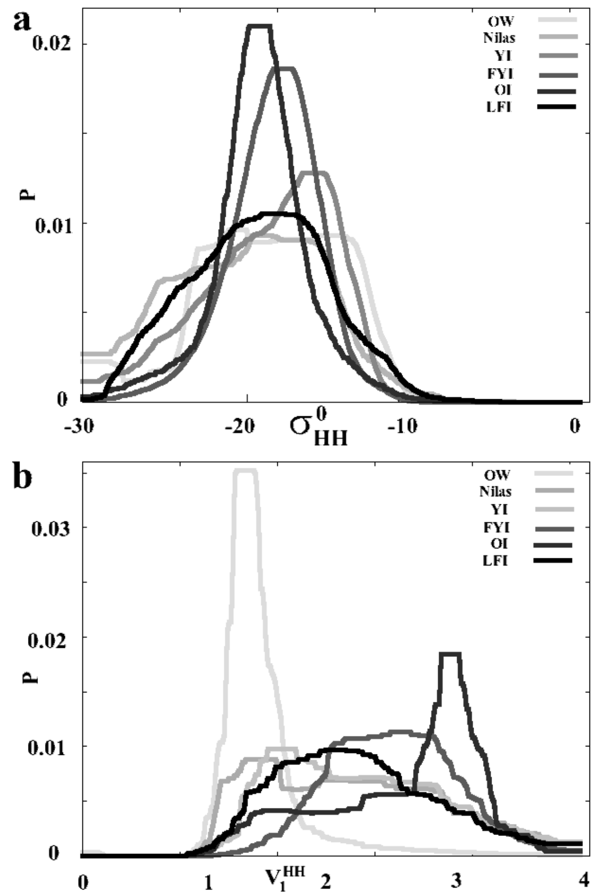

Fig. 10. (a) Class-wise histograms for the L-band HH σ^0 and (b) HH variogram slope.

D. SI Drift

In [33], SID estimation over the Baltic SI using the C- and L-band single-polarization (HH) image pairs, including mixed L- and C-band pairs, was evaluated. The method used was a pairwise cross correlation. According to the results, a pair of two L-band SAR images was found to be the best option, a pair of two C-band images also performed well, and a mixed C-/L-band pair performed worse but was still found to give useful ice drift estimates. In our ALOS-2/PALSAR-2 test data set, there were not many suitable image pairs for ice drift estimation testing. We found only one overlapping image pair with a reasonable time difference and some detectable ice drift in our data set. This image pair has almost a three-day time difference between the acquisitions; the acquisition times were March 20, 2017, 20:05:19 UTC and March 23, 2017, 14:28:57. We applied the algorithm presented in [34] to this image pair using linear combinations of the HH and HV channels as inputs. The weights of the linear combination between HH and HV channels were defined based on PCA. The algorithm produced an ice drift field in

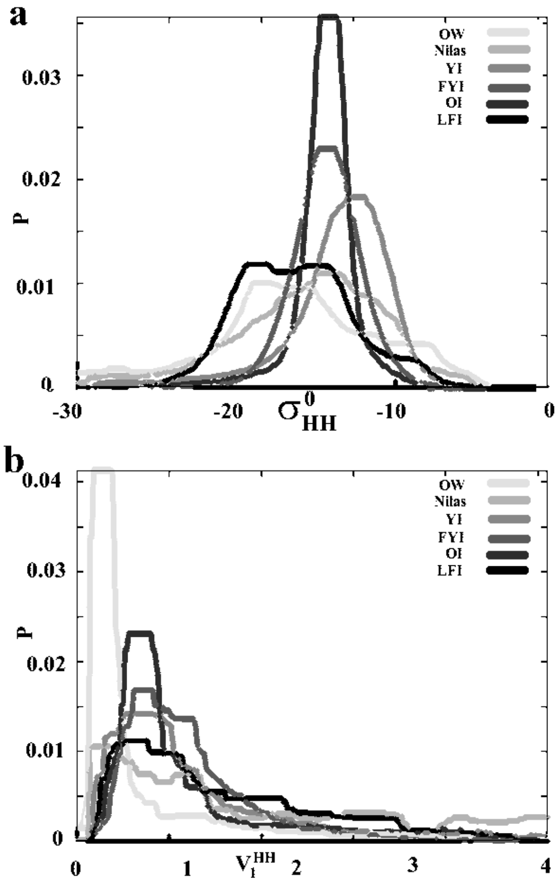

Fig. 11. (a) Class-wise histograms for the C-band HH σ^0 and (b) HH variogram slope.

agreement with our visual interpretation. The visual evaluation was made by selecting points that could visually be identified in both the images of the image pair and their location was manually defined. The points were selected over different areas of the image pair. Then, the visually detected motion was defined as a difference between the location coordinates of the corresponding points in the two images. The differences between the visually estimated drift and the drift produced by the algorithm were in the range of 0–2 pixels (0–200 m), which corresponds to the accuracy of the visual detection of the locations. Based on this evaluation, we can say that the ice drift detection algorithm performed well for this L-band SAR image pair, thus supporting the understanding that L-band data are well suitable for SI drift estimation. The UL and LR corners of the image are (81.8°1N, 2.54° E) and (81.38°N, 26.26° E), respectively. The locations of the two images within our study area are shown in Fig. 13, and the images also cover areas located north of Svalbard. The image pair and the resulted drift vectors are shown in Fig. 14.

VI. Discussion

We have studied the potential of L-band data for SI monitoring with a data set from ALOS-2/PALSAR-2. To evaluate the SI parameter estimation results, reliable reference data would be required. However, in general, SI *in situ* reference measurements over the Arctic for method evaluation is in practice missing, and we only have SI parameter and classification data derived from the measurements of other earth observation (EO) instruments. In practice, we have their visual interpretations, mainly in the form of gridded ice charts, at our disposal. Actual *in situ* measurements on ice fields are difficult and laborious to perform, and for this reason, very little such measurements over Arctic exist. Even the existing *in situ* data also are very local (both in space and time), and for example, even the few Russian SI measurement are very difficult to obtain.

It should be noticed that the ALOS-2/PALSAR-2 ScanSAR HV-channel processing parameterization was changed on April 11, 2018: the onboard ATT (attenuator) setting was changed from 25 to 20 dB. Before changing this setting, ScanSAR HV-polarization images sometimes became dark and blurred over ocean and coastal regions [35]. As the imagery of this article has been acquired in 2017, this degradation at the HV channel also applies to the imagery used in this article and may have affected negatively on the HV band classification and estimation results presented.

SI/OW classification and SIC estimation can be performed quite reliably based on dual-polarized SAR imagery. The results at L-band are quite similar to the earlier results using C-band SAR, e.g., in [8]. Especially, the MLP approach for estimating SIC from L-band dual-polarized SAR data gave promising results, comparable or even slightly better compared with those using C-band SAR data. Even better SIC estimation results can be achieved by combining multiple SAR features or even combining with MWR data. One approach to combine C-band SAR features and AMSR2 MWR brightness temperature gradient and polarization ratios for the Baltic SI is presented in [12]. According to this study, the L1 error of the SIC estimates was reduced by about five percentage points by including the MWR data in the estimation. The reference SIC in the Baltic Sea study was the SIC of the gridded FMI Baltic SI charts. Also, other approaches to combine SAR and MWR for SIC estimation have been proposed, such as the data assimilation approach presented in [36]. However, based on the experiments performed, SIC can, in most cases, be estimated solely from L-band dual-polarized SAR data well enough, e.g., for SI navigation. The problems occur in warm conditions with wet snow or liquid water on SI, i.e., during the melting period. According to our visual analysis, L-band SAR can estimate SIC better than MWR that underestimates SIC during the melting period.

More realistic prior probabilities would very likely improve the Bayesian OW/SI classification mentioned in Section V-A because now we have applied equivalent prior probabilities of 0.5 for both the classes; this is not realistic in most cases, in the midwinter time, ice is more probable than OW and in the freeze-up and melting period, OW is more dominant. The probabilities in different areas also differ, e.g., in general, ice is more probable in the north than in the south. The prior probabilities of the two classes could also be varied according to the area and time of the year using a representative historical data set to define meaningful prior probabilities. By applying a (linear or nonlinear) combination of the features, at least

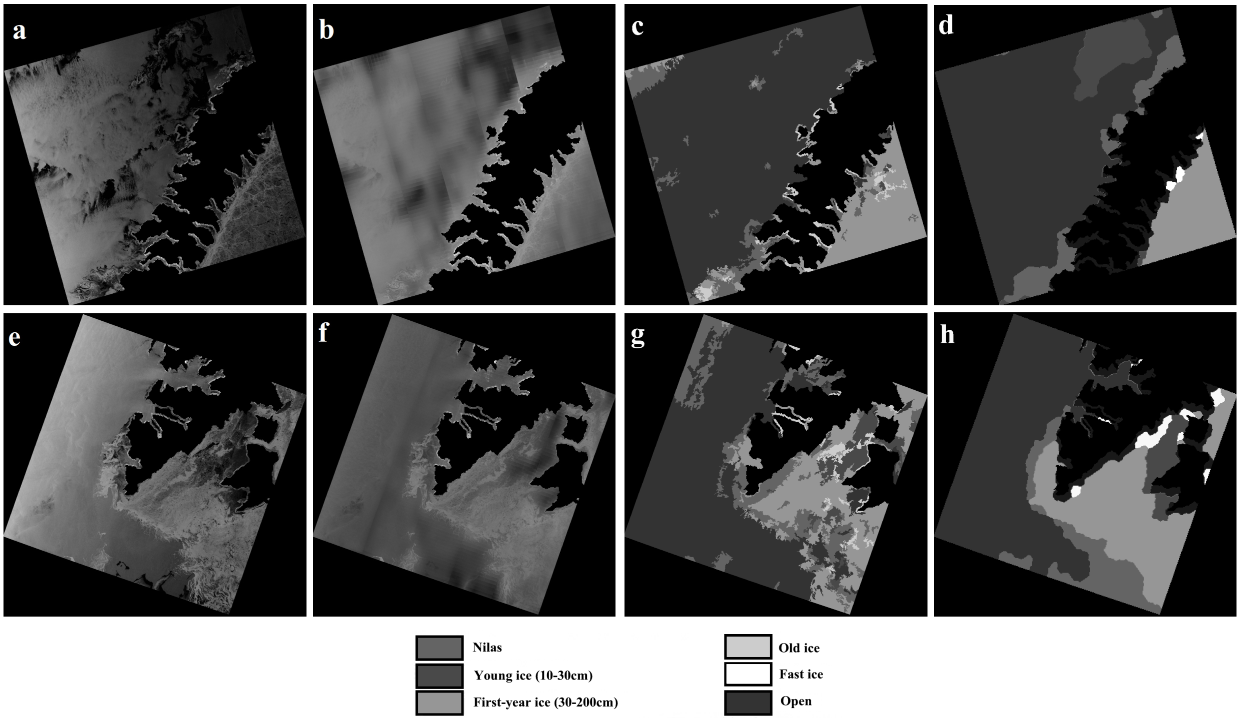

Fig. 12. (a) and (e) HH and (b) and (f) HV SAR images of (c) and (g) two SAR images FMI classification, and (d) and (h) AARI ice types corresponding to two SAR images. Both SAR images shown were acquired on April 18, 2017.

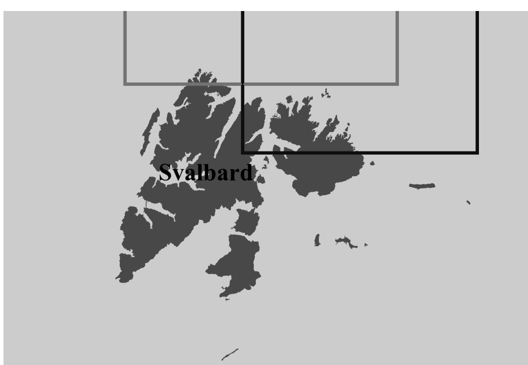

Fig. 13. Locations of the ALOS-2/PALSAR-2 image pair used in testing ice drift estimation. The images only partly overlap with the study area, but whole images were used in the ice drift estimation experiment.

similar accuracies as using C-band in SI/OW discrimination [24], [37] and SIC estimation can be achieved. There also probably exist some inaccuracies in the reference data set. More accurate reference data set would lead to more accurate and consistent estimates. SIC estimation at a high resolution is also possible using the SI/OW classification methods and counting the proportions of the OW and SI grid points either within a sliding window or within SAR segments.

According to this study, SI classification into four classes in the AARI ice charts using a single SAR texture feature is possible according to the histograms shown in Fig. 10(b). However, according to the histogram figure, perfect classification is not possible, but the classes are only partially separable, and some overlaps between the classes exist. These overlaps are at least partially due to the spatially coarse classification provided in the ice charts (small details are ignored in manual classification and the classes assigned to rather large polygons in the ice charts). This can, for example, be seen in the examples of C-band SAR classification and their comparison to the ice chart classification given in [38]. Also, different classification schemes from the classification in AARI ice charts would be more favorable for SAR-based SI classification. SI SAR imagery could, for example, be classified based on degree of SI deformation. The degree of SI deformation from L-band SAR data should still be studied in more detail. According to our experience in the Baltic Sea, degree of ice deformation is a better suitable parameter to be estimated from SAR data than the ice classes given by ice charts [31]. Using more realistic prior probabilities in the Bayes classification could improve the classification, but as for SI/OW classification, a large comprehensive historical data set would be required to capture the seasonal and spatial variations.

Our SIT estimation algorithm was trained and tested with CS-2 data assigned to SAR segments. In addition, we used the SIT reference data from TOPAZ4 ice model and AARI ice charts. We have noticed that SIT reference data given by the TOPAZ4 ice model are not very accurate and they do not have much local variation, in practice giving only very large-scale average SIT forecasts. The same applies to the AARI ice chart polygons; they are rather coarse lacking details. The comparisons showed rather low correlations, but the L1 differences with respect to reference data were reasonable. Also, visual comparison of the SIT results with the reference SIT data

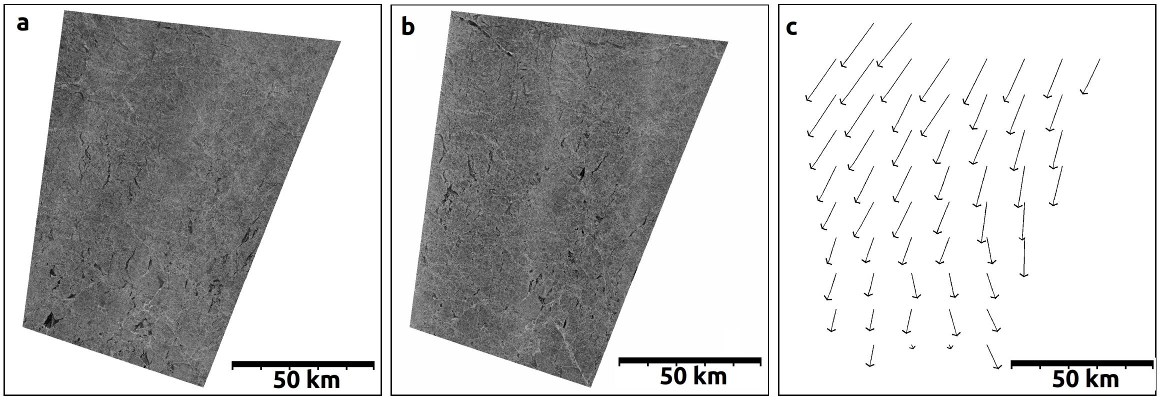

Fig. 14. Overlapping areas of the PALSAR-2 images of (a) March 20, 2017, 20:05:19 UTC and (b) March 23, 2017, 14:28:57 UTC and (c) corresponding ice drift vector field between the acquisitions. The SAR images gray scales have been normalized for better visual quality. The vector field is presented in sparse resolution, and the vectors have been scaled longer for better visual quality. The dominant ice drift direction is to south/southwest.

looks reasonable, locations of thin ice and thick ice fields agree quite well, and the SAR SIT just contains more details than the reference data. SI volume can be estimated from SIC and SIT by integrating, or summing in the case of a discrete grid, the product of SIC and SIT over a desired area. Based on the uncertainty estimates for SIC and SIT, we can also derive rough uncertainty estimates for ice volume estimation. Based on L-band data, we could estimate ice volume over our study area with an uncertainty of 20%–30% depending on the prevailing ice conditions (SIC and SIT). This number indicates that dual-channel L-band SAR data and the presented methods are not very accurate for ice volume estimation but perform better than C-band SAR data anyway. A better and more accurate solution for SIT estimation would be to use a combination of multiple instruments, e.g., SAR, altimeter, and MWR. An SIT estimation method combining data from C-band SAR, MWR, and TOPAZ4 ice model was proposed in [26], but more preferable would be to replace the model data by altimeter data to get an SIT product based solely on the EO data.

According to an earlier study [33], ice drift can rather reliably be estimated from L-band SAR data. Here, we were only able to make a test with one image pair, and the result supports the earlier observations. For our data set, SID could only be estimated over the common areas of one SAR image pair and the estimates were in agreement with the visually observed drift. A major problem related to ALOS-2/PALSAR-2 ice drift detection is that the temporal resolution of the currently available L-band data over Arctic is most of the time all too coarse for ice drift detection. A benefit of any available L-band data would be that they could also be used for SID estimation in combination with C-band SAR data (mixed image pairs), and thus, they could also be used as complementary data in the ice drift estimation for the already existing operational C-band missions.

All the test were run on a Linux workstation with 24 Intel Xeon X5650 cores running at 2.67-GHz clock speed and with 48 GB of RAM. The software was not designed to run in parallel and thus was also executed in only one CPU core sequentially. The execution times for one classification or one parameter estimation were a few minutes or less, indicating that the proposed methods can, in this respect, directly as such be used for operational SI monitoring.

VII. Conclusion

In this article, we have explored the suitability of ALOS-2/PALSAR-2 dual-polarized L-band SAR data for Arctic SI remote sensing. We studied the classification of SI into ice classes provided by ice charts, distinguishing between OW and SI, and estimation of three essential SI parameters: SIC, SIT, and SID.

This article clearly shows that the L-band data are well suitable for Arctic SI parameter estimation and classification. The study was made in a study area in Kara and Barents seas and there was not much multiyear (second year or older ice) present, and the capability to distinguish between FYI and multiyear ice is thus based on a rather limited amount of grid points (image pixels in 500-m resolution). However, according to this limited data set, it seems that the SI class of "OI," corresponding to SI older than one year, was rather well distinguished from many other ice classes even using a single texture feature (HH channel variogram slope, V_1^{HH}). Based on this study, it can be said that the L-band dual-polarized (HH/HV) SAR data can be used to estimate SIC and SIT with equal or better performance than the corresponding C-band data. Also, SI classification results using a simple single texture feature approach were better than those for C-band. C-band performance was here evaluated only based on the class-wise feature histograms that had more overlap between the classes than L-band feature histograms. Also, ice drift can be reliably estimated using the multitemporal L-band SAR data according to our experience. The slightly better performance of L-band SAR compared to C-band is likely due to the deeper penetration of L-band and thus backscatter from a larger volume than for C- and X-bands.

JAXA's ALOS-2/PALSAR-2 is a research instrument, and the typical delays from image acquisition to user are too long for the near-real-time requirements of, e.g., ice navigation. Also, the spatiotemporal coverage of only one SAR satellite, even if operated continuously over the Arctic, is too restricted for operational monitoring alone. Current ALOS-2/PALSAR-2 makes acquisitions only during a few short-time campaigns over the Arctic in a year. However, L-band data could even now be used more in operational SI monitoring to complement the data available from operational C-band and X-band instruments. A preferable alternative would be an operational L-band SAR mission or rather a constellation of two or more satellites carrying L-band SAR instruments.

In the future studies, using nonlinear methods and iterative self-focusing algorithms in SI parameter estimation will be studied more. Also, joint use of L- and C-band data for improved SI parameter estimation would need more investigation. Additional comparisons between L- and C-band, possibly also X-band, data will be needed, also including more detailed comparisons between C-band texture, L-band texture, and joint texture (e.g., cross correlations between nearly simultaneous coregistered different frequency bands) measures, and also including more texture measures, e.g., multiscale features, such as fractal dimension, and segment-wise corner point densities, such as in [12].

Methods using multitemporal SAR data over the same area should be studied more because they give information on changes (ice drift and deformation) and indicate the static ice areas. Multitemporal data can also be used to reduce the noise in SAR imagery by applying multitemporal filtering (e.g., median) over the same ice field recognized in many SAR images acquired at different time instants. This would require accurate tracking of the ice fields if they are moving. Multitemporal filtering is easier to be applied to static SI areas, such as LFI [32]. However, this would also require a significantly higher temporal resolution than we have with the currently available L-band data set.

REFERENCES

[1] W. Dierking and T. Busche, "Sea ice monitoring by L-band SAR: An assessment based on literature and comparisons of JERS-1 and ERS-1 imagery," *IEEE Trans. Geosci. Remote Sens.*, vol. 44, no. 4, pp. 957–970, Apr. 2006.

[2] L. E. B. Eriksson *et al.*, "Evaluation of new spaceborne SAR sensors for sea-ice monitoring in the baltic sea," *Can. J. Remote Sens.*, vol. 36, no. 1, pp. S56–S73, Jan. 2010.

[3] L. E. B. Eriksson *et al.*, "Evaluation of multi-polarization SAR data at L-, C-, and X-band for sea-ice monitoring in the baltic sea," in *Proc. ESA Living Planet Symp.*, Bergen, Norway, vol. 686, Jun./Jul. 2010.

[4] J. A. Karvonen, "Baltic sea ice SAR segmentation and classification using modified pulse-coupled neural networks," *IEEE Trans. Geosci. Remote Sens.*, vol. 42, no. 7, pp. 1566–1574, Jul. 2004.

[5] J. Karvonen, "C-band sea ice SAR classification based on segmentwise edge features," *Geosci. Remote Sensing New Achievements*. Rijeka, Croatia: InTech, 2010, pp. 129–146.

[6] J. Karvonen, B. Cheng, T. Vihma, M. Arkett, and T. Carrieres, "A method for sea ice thickness and concentration analysis based on SAR data and a thermodynamic model," *Cryosphere*, vol. 6, no. 6, pp. 1507–1526, 2012.

[7] J. Karvonen, "Baltic sea ice concentration estimation based on C-band HH-polarized SAR data," *IEEE J. Sel. Topics Appl. Earth Observ. Remote Sens.*, vol. 5, no. 6, pp. 1874–1884, Dec. 2012.

[8] J. Karvonen, "Baltic sea ice concentration estimation based on C-band dual-polarized SAR data," *IEEE Trans. Geosci. Remote Sens.*, vol. 52, no. 9, pp. 5558–5566, Sep. 2014.

[9] J. C. Comiso, "Characteristics of arctic winter sea ice from satellite multispectral microwave observations," *J. Geophys. Res.*, vol. 91, no. C1, pp. 975–994, 1986.

[10] R. L. Tilling, A. Ridout, and A. Shepherd, "Estimating Arctic sea ice thickness and volume using CryoSat-2 radar altimeter data," *Adv. Space Res.*, vol. 62, no. 2, pp. 1203–1225, 2018.

[11] P. Sakov, F. Counillon, L. Bertino, K. A. Lisæter, P. R. Oke, and A. Korablev, "TOPAZ4: An ocean-sea ice data assimilation system for the North Atlantic and arctic," *Ocean Sci.*, vol. 8, no. 4, pp. 633–656, 2012.

[12] J. Karvonen, "Baltic sea ice concentration estimation using SENTINEL-1 SAR and AMSR2 microwave radiometer data," *IEEE Trans. Geosci. Remote Sens.*, vol. 55, no. 5, pp. 2871–2883, May 2017.

[13] (2014). *JCOMM (Joint World Meteorological Organization (WMO) Intergovernmental Oceanographic Commission (IOC) Technical Commission for Oceanography and Marine Meteorology), SIGRID-3: A Vector Archicve Format for Sea Ice Charts, JCOMM-TR-023, Revision 3*. Accessed: Feb. 1, 2020. [Online]. Available: https://www.jcomm.info/index.php?option=com_oe&task=viewDocumentRecord&docID=4439

[14] *WMO Egg Code Description*. [Online]. Available: http://www.natice.noaa.gov/products/egg_code.html

[15] S. Sandven and O. M. Johannesen, "Sea ice monitoring by remote sensing," in *Manual of Remote Sensing: Remote Sensing of the Marine Environment*, vol. 6, 3rd ed., F. R. G. James, Ed. Bethesda, MD, USA: American Society for Photogrammetry & Remote Sensing, 2006, pp. 241–283.

[16] *ALOS-2/PALSAR-2Level 1.1/1.5/2.1/3.1 CEOS SAR Product Format Description*, JAXA, Tokyo, Japan, May 2014.

[17] J. Karvonen, "A sea ice concentration estimation algorithm utilizing radiometer and SAR data," *Cryosphere*, vol. 8, no. 5, pp. 1639–1650, 2014.

[18] J. Karvonen, "Evaluation of the operational SAR based baltic sea ice concentration products," *Adv. Space Res.*, vol. 56, no. 1, pp. 119–132, Jul. 2015.

[19] M. Makynen and J. Karvonen, "Incidence angle dependence of first-year sea ice backscattering coefficient in Sentinel-1 SAR imagery over the kara sea," *IEEE Trans. Geosci. Remote Sens.*, vol. 55, no. 11, pp. 6170–6181, Nov. 2017.

[20] P. Wessel and W. H. F. Smith, "A global, self-consistent, hierarchical, high-resolution shoreline database," *J. Geophys. Res., Solid Earth*, vol. 101, no. B4, pp. 8741–8743, Apr. 1996.

[21] J. Besag, "On the statistical analysis of dirty pictures," *J. Roy. Stat. Soc. B, Methodol.*, vol. 48, no. 3, pp. 259–279, Jul. 1986.

[22] C. E. Shannon, "A mathematical theory of communication," *Bell Syst. Tech. J.*, vol. 27, p. 379–423, 623–656, 1948.

[23] M. Simila, "SAR image segmentation by a two-scale contextual classifier," in *Proc. SPIE, Conf. Image Signal Process. Remote Sens.*, vol. 2315, J. Desachy, Ed. 1994, pp. 434–443.

[24] J. Karvonen, M. Simila, and M. Makynen, "Open water detection from baltic sea ice Radarsat-1 SAR imagery," *IEEE Geosci. Remote Sens. Lett.*, vol. 2, no. 3, pp. 275–279, Jul. 2005.

[25] N. Cressie, *Statistics for Spatial Data*. New York, NY, USA: Wiley, 1993, pp. 69–101.

[26] M. Similä, M. Mäkynen, B. Cheng, and E. Rinne, "Multisensor data and thermodynamic sea-ice model based sea-ice thickness chart with application to the kara sea, arctic Russia," *Ann. Glaciol.*, vol. 54, no. 62, pp. 241–252, 2013.

[27] E. Kalnay *et al.*, "The NCEP/NCAR 40-year reanalysis project," *Bull. Amer. Meteorol. Soc.*, vol. 77, Mar. 1996, pp. 437–470, doi: 10.1175/1520-0477(1996)077<0437:TNYRP>2.0.CO;2.

[28] J. C. Comiso and C. L. Parkinson, "Arctic sea ice parameters from AMSR-E data using two techniques and comparisons with sea ice from SSM/I," *J. Geophys. Res.*, vol. 113, no. C2, pp. 1–16, 2008, doi: 10.1029/2007JC004255.

[29] S. Hendricks, R. Ricker, and V. Helm, "User guide: AWI CryoSat-2 sea ice thickness data product (v1.2)," Alfred Wegener Inst. (AWI), Bremerhafen, Germany, Eprint ID 41242, 2016.

[30] J. Stewart, *Multivariable Calculus*, 3rd Ed. Pacific Grove, CA, USA: Brooks/Cole, 1995, p. 790.

[31] A. Gegiuc, M. Similä, J. Karvonen, M. Lensu, M. Mäkynen, and J. Vainio, "Estimation of degree of sea ice ridging based on dual-polarized C-band SAR data," *Cryosphere*, vol. 12, no. 1, pp. 343–364, 2018.

[32] J. Karvonen, "Estimation of arctic land-fast ice cover based on dual-polarized Sentinel-1 SAR imagery," *Cryosphere*, vol. 12, no. 8, pp. 2595–2607, 2018.

[33] J. Lehtiranta, S. Siiriä, and J. Karvonen, "Comparing C- and L-band SAR images for sea ice motion estimation," *Cryosphere*, vol. 9, no. 1, pp. 357–366, Feb. 2015, doi: 10.5194/tc-9-357-2015.

[34] J. Karvonen, "Operational SAR-based sea ice drift monitoring over the baltic sea," *Ocean Sci.*, vol. 8, no. 4, pp. 473–483, 2012.

[35] (2018). *JAXA (Japan Aerospace Exploration Agency), Change of SAR Attenuator Setting for ScanSAR HV Mode*. Accessed: Mar. 23, 2020. [Online]. Available: https://www.eorc.jaxa.jp/ALOS-2/en/calval/PALSAR2_ScanSAR_ATT_change_201808.pdf

[36] N. G. Kasapoglu, "Sea ice concentration retrieval using composite ScanSAR features in a SAR data assimilation process," *IEEE Geosci. Remote Sens. Lett.*, vol. 11, no. 12, pp. 2085–2089, Dec. 2014.

[37] J. Karvonen, "A comparison of two C-band SAR ice/open water algorithms," in *Proc. ESA SeaSAR Workshop*, 2010.

[38] J.-W. Park, A. A. Korosov, M. Babiker, J.-S. Won, M. W. Hansen, and H.-C. Kim, "Classification of sea ice types in sentinel-1 SAR images," submitted for publication, doi: 10.5194/tc-2019-127.

Juha Karvonen (Member, IEEE) received the M.Sc. (Tech.), Lic.Tech., and Dr.Sc. (Tech.) degrees in information and computer sciences and digital signal processing from the Helsinki University of Technology (Aalto University since 2010), Espoo, Finland, in 1991, 1996, and 2006, respectively. His Dr.Sc. thesis was dealing with remote sensing of sea ice by SAR.

He was in the field of industrial machine vision. He has been involving in the field of earth observation and remote sensing since 1997. He is currently a Senior Research Scientist with the Remote Sensing Research Group and Finnish Ice Service, which are parts of the Finnish Meteorological Institute, Helsinki, Finland, developing earth observation (EO) products for winter navigation. His research interests include digital signal and image processing, SAR and other EO data processing, sea ice, and operational marine services.

Eero Rinne received the M.Sc. (Tech.) degree in space technology from the Helsinki University of Technology, Helsinki, Finland, in 2005, and the Ph.D. degree in geophysics from the University of Edinburgh, Edinburgh, U.K., in 2011.

He has been leading the Polar Oceanography and Sea Ice Research Group, Finnish Meteorological Institute, Helsinki, since 2013. His scientific career has concentrated on satellite remote sensing of the cryosphere, including terrestrial snow, glaciers, and sea ice.

Heidi Sallila received the M.Sc. (Tech.) degree in geoinformatics from Aalto University, Espoo, Finland, in 2016. She is currently pursuing the Ph.D. degree in geophysics while working in the Polar Oceanography and Sea Ice Group, Finnish Meteorological Institute, University of Helsinki, Helsinki, Finland.

Her main field is satellite altimetry of sea ice thickness.

Marko Mäkynen (Member, IEEE) received the D.Sc. (Tech.) degree from the Helsinki University of Technology (TKK) (Aalto University since 2010), Espoo, Finland, in 2007.

From 1999 to 2006, he was a Senior Teaching Assistant with the Laboratory of Space Technology, TKK, where he was the Acting Director from 2007 to 2008. Since 2009, he has been a Senior Scientist with the Marine Research Unit, Finnish Meteorological Institute, Helsinki, Finland. He is currently an Adjunct Professor in microwave remote sensing with Aalto University. His research interests include microwave and optical remote sensing of the Baltic sea ice and Arctic sea ice and the development of operational marine services.